The 2020 M_w 6.8 Elazığ (Turkey) earthquake reveals rupture behavior of the East Anatolian Fault

Léa Pousse-Beltran[1], Edwin Nissen[1], Eric A. Bergman[2], Musavver Didem Cambaz[3], Élyse Gaudreau[1], Ezgi Karasözen[4], and Fengzhou Tan[1]

[1]School of Earth and Ocean Sciences, University of Victoria, Victoria BC, Canada
[2]Global Seismological Services, Golden CO, USA
[3]Kandilli Observatory and Earthquake Research Institute, Boğaziçi University, İstanbul, Turkey
[4]Alaska Earthquake Center, University of Alaska Fairbanks, Fairbanks AK, USA

Key Points:

- The mainshock propagated bilaterally from a nucleation point on an abrupt ∼10° fault bend
- Only one rupture termination corresponds to an established EAF segment boundary, and the rupture may partially overlap with an 1874 earthquake
- The mainshock exhibits a pronounced shallow slip deficit, that is not fully recovered through early shallow afterslip

Corresponding author: Léa Pousse-Beltran, `leapousse@uvic.ca`

Abstract

The 2020 M_w 6.8 Elazığ earthquake was the largest along the Eastern Anatolian Fault (EAF) in over a century and so provides valuable insights into its rupture behavior. Because the EAF is of low-to-intermediate structural maturity, this earthquake could also help refine the controls of cumulative fault offset on characteristics such as rupture velocity, shallow slip deficits, and afterslip. We use satellite geodesy and seismology to detail the mainshock rupture, postseismic deformation and aftershocks, and relations to previous earthquakes. The mainshock propagated bilaterally at ∼2 km/s from a nucleation point on an abrupt ∼10° fault bend. Only one end of the rupture corresponds to an established EAF segment boundary, and the earthquake may have propagated into the slip zone of the 1874 M ∼7.1 Gölcuk Gölu earthquake. It exhibits a pronounced (∼80%) shallow slip deficit, only a small proportion of which is recovered by early aseismic afterslip.

1 Introduction

The left-lateral East Anatolian Fault (EAF) in southeastern Turkey forms the active plate boundary between Arabia and Anatolia (Figure 1a, b). Striking ∼WSW between the Karlıova triple junction at ∼41° E and the Dead Sea Transform at ∼36° E — a total distance of ∼500 km — the EAF encompasses several releasing and restraining bends, stepovers, and oblique splay faults (Arpat & Şaroğlu, 1972; Bozkurt, 2001). The segmentation of the EAF is likely influenced by its obliquity to E–W structures of the SE Anatolia Thrust Zone, part of the Bitlis-Zagros suture zone (Şengör & Yilmaz, 1981; Yılmaz, 1993). Together with the conjugate, right-lateral North Anatolian Fault (NAF), the EAF accommodates westward extrusion of Anatolia from the Arabia-Eurasia collision zone (McKenzie, 1972; Jackson & McKenzie, 1984). Both faults are associated with numerous destructive historical earthquakes (Ambraseys & Jackson, 1998), but whereas the NAF has hosted a dozen $M_w \geq 6.7$ ruptures during the past century (Stein et al., 1997; Tibi et al., 2001), the EAF is characterized by a notable scarcity of large instrumental events. This has hampered our understanding of its kinematics, structural characteristics and rupture behavior.

The January 24 2020 M_w 6.8 Elazığ earthquake struck at 17:55 UTC (20:55 local time) and caused extensive damage across the southern Elazığ and Malatya provinces, killing ∼41 people and injuring ∼1,600 others. It was the largest earthquake on the EAF in more than a century, motivating a detailed examination of its rupture characteristics. Nucleating close to Lake Hazar, a contested segment boundary along the central EAF (Figure 1c), the Elazığ earthquake can potentially help resolve uncertainties in local fault structure and its controls on rupture propagation (Barka & Kadinsky-Cade, 1988; Aksoy et al., 2007; Garcia Moreno et al., 2011; Duman & Emre, 2013). Furthermore, since the 2020 earthquake lies between large historical earthquakes in 1874 and 1875 (to the NE) and 1893 and 1905 (to the SW) (Ambraseys (1989); Figure 1b), it could help inform broader controversies over continued application of the characteristic earthquake and seismic gap models (Parsons & Geist, 2009; Kagan et al., 2012; Mulargia et al., 2017). Finally, since the central EAF is well-characterized as of low-to-intermediate structural maturity — with a slip-rate of ∼11 mm/yr (Cetin et al., 2003; Walters et al., 2014; Aktug et al., 2016) and cumulative geomorphological or geological offsets of ∼9–26 km (Duman & Emre, 2013) — the 2020 earthquake could help refine relations between fault structural maturity and characteristics such as rupture velocity, off-fault deformation, shallow slip deficits, and afterslip (e.g., Dolan & Haravitch, 2014; Socquet et al., 2019; Li et al., 2020).

The main goal of this paper is to characterize the Elazığ mainshock faulting and its early aftershock activity and postseismic deformation. We do so by synthesizing geodetic and seismological data and techniques including Interferometric Synthetic Aperture Radar (InSAR) imagery and elastic dislocation models, teleseismic back-projections, regional moment tensor (RMT) analyses, and calibrated hypocentral relocations. We also discuss relations between the 2020 earthquake and proposed segment boundaries models for the central EAF, historical earthquake ruptures, and background instrumental seismicity. Finally, we consider the Elazığ earthquake in the context of controls of fault structural maturity on rupture behavior.

2 Methods

2.1 Satellite geodesy

We investigated coseismic and postseismic deformation in the 2020 Elazığ earthquake using European Space Agency (ESA) Sentinel-1 interferograms on ascending tracks 43A and 116A and descending tracks 21D and 123D (for dates, see Supplementary Table S1). We estimated the mainshock fault geometry and slip distribution using a well-established elastic dislocation modeling approach (e.g., Wright et al., 1999; Elliott et al., 2012). After downsampling the unwrapped interferograms with a Quadtree algorithm (Jónsson et al., 2002), we used Powell's algorithm with multiple Monte Carlo restarts (Press et al., 1992; Clarke et al., 1997) to solve for the minimum misfit source parameters of a rectangular fault plane embedded within an elastic half-space (Okada, 1985), together with E–W and N–S orbital ramps and the zero displacement level. Details of the elastic parameters are given in Supplementary Text S1. Ascending and descending data were given equal weighting in the inversion, but track 21D was weighted one third relative to 123D since it only spans that fraction of the rupture. We then extended and subdivided the model fault plane into 3 × 3 km subfaults and solved for the slip and rake distribution, ensuring realistic gradients by applying a Laplacian smoothing operator (Wright et al., 2003).

Postseismic interferograms revealed shallow afterslip along the rupture trace, but the relatively low signal-to-noise ratio precluded us applying the same inversion procedure as for coseismic slip. Instead, we estimated afterslip at intervals along strike and through time from fault-perpendicular displacement profiles. We computed three-dimensional displacement components from tracks 43A, 116A, and 123D, and projected them onto the 244°-oriented fault. Assuming that all the deformation is horizontal and fault parallel, we can model the displacement (y) at perpendicular distance (x) from the fault with an arctan function to solve for uniform slip U and locking depth D (Savage & Burford, 1973). Adding a linear term ($R \times x$) to account for residual orbital ramps, we obtained a function model $y = \frac{U}{\pi} \times \arctan(\frac{x}{D}) + Rx$, that we fitted using the least squares Levenberg-Marquardt algorithm (Moré, 1978). We used the same elastic half-space parameters as for the coseismic modeling (Supplementary Text S1).

We also investigated horizontal surface deformation using an optical image correlation (OIC) of pre- and post-earthquake ESA Sentinel-2 images. OIC can detect near-fault surface deformation caused by shallow slip in regions where radar interferograms often decorrelate, and can thus help refine InSAR slip models (Xu et al., 2016; Scott et al., 2019). Unfortunately, the epicentral region was obscured by dense cloud cover after the earthquake with the earliest usable post-seismic image collected on February 27 2020; our results therefore capture both coseismic and five weeks of postseismic deformation. The pre-event image was acquired on November 9 2019 and was chosen based on the similar illumination conditions and the clear view of the study area. Level 1C (orthorectified) images from ESA with a 10-m resolution (band 8) were correlated using the frequency correlator in the COSI-Corr software (Leprince et al., 2007). A multi-scale sliding correlation window (64 pixels to 32 pixels) was used with a step of 4 pixels, thus the resulting map of subpixel horizontal displacements has a 40-m pixel resolution. Noise in the displacement maps is reduced by removing outliers and applying a non-local means filter, using a 5-pixel by 5-pixel patch size, 21-pixel area, and a noise parameter value of 2 and 2.25 (Ayoub et al., 2017).

2.2 Seismology

We imaged the mainshock rupture propagation using a phase-weighted relative back projection based upon high-frequency P waves recorded across a teleseismic station array (Ishii et al., 2005; F. Tan et al., 2019). After trials with data from a number of regions, we settled upon an Alaskan array comprising 119 stations with high cross-correlation coefficients for the first few seconds of the P wave and at distances of 69–86°. Theoretical travel times were calculated linking a grid of nodes across the source region to each station (Supplementary Text S1). Waveforms were cleaned with a 0.3–2 Hz band-pass filter. Assuming a source depth of 6 km — consistent with our InSAR modeling results — we mapped relative energy at 1 s intervals and a 10 s sliding window for the duration of the rupture.

We estimated source mechanisms of fifteen early aftershocks (up to February 17 2020) by modeling regional waveforms recorded up to 350 km away at stations of the Kandilli Observatory and Earthquake Research Institute (KOERI) seismic network (Boğaziçi University Kandilli Observatory and Earthquake Research Institute, 2001). To ensure good azimuthal coverage, at least six stations were used for each event. Seismograms were filtered between 0.02–0.09 Hz, with the exact frequency band for each event selected after analyzing signal-to-noise ratios and station epicentral distances. Green's functions were estimated for the local velocity model (Supplementary Text S1) using the discrete wavenumber method of Bouchon (1981) and Bouchon (1981). We solved for the best single- or multiple-point source representation of each earthquake using the iterative deconvolution inversion method (Kikuchi & Kanamori, 1991) implemented in the ISOLA software package (E. N. Sokos & Zahradník, 2008; E. Sokos & Zahradník, 2013). Sub-event moment tensors were estimated by a least squares minimization of misfits between observed and synthetic waveforms, while sub-event positions and relative times were determined through grid search (Zahradník et al., 2005).

Finally, we used local, regional and teleseismic phase arrivals to relocate hypocenters of the mainshock, 30 early aftershocks (up to February 20 2020), and ∼300 well-recorded background events starting in 1971. Data were gathered from regional networks operated by AFAD, KOERI and the European-Mediterranean Seismological Centre (EMSC), as well as from the International Seismological Centre (ISC) bulletin. Target earthquakes were separated into five distinct clusters: the first focused on the 2020 sequence together with potential foreshock activity during 2019; a second targeted earlier seismicity along the Pürtürge segment of the EAF; and a third, fourth and fifth targeted events on segments to the ENE and WSW (Supplementary Figure S1a). Each cluster was relocated using the *mloc* program (Bergman & Solomon, 1990; Walker et al., 2011), which divides the relocation procedure into two distinct inverse problems reliant on customized phase arrival time data (Jordan & Sverdrup, 1981). Firstly, arrival times of all phases at all distances were used to determine 'cluster vectors' that relate individual locations and origin times to the hypocentroid (the geometrical mean for all events). Secondly, direct Pg and Sg phases at epicentral distances of $<1°$ are used to establish the absolute location and origin time of the hypocentroid, thus yielding 'calibrated' hypocenters (Karasözen et al., 2016). Crustal velocity models appropriate to each cluster were determined by analyzing fits to Pg and Pn at the closest stations and Pn and Sn at regional distances (Supplementary Text S1 and Figure S1b).

3 Results

3.1 Background seismicity and foreshock activity

Full calibrated earthquake relocation results are plotted in Supplementary Figure S1 and listed in Tables S2–S6. A large number of events are relocated to on or adjacent to the Pürtürge segment of the EAF, including eight of M_w 4.9–5.7 which are sufficiently well-recorded as to be ascribed teleseismic focal mechanisms (Figures 1b–c, Figure 2a). Four of these moderate earthquakes have predominantly strike-slip mechanisms and form a linear trend ∼5 km north of the main fault surface trace. This distance exceeds the relocation uncertainties, hinting at a previously unrecognized northern strand of the Pürtürge segment of the EAF. We also observe one moderate and several smaller earthquakes south of the town of Sivrice, consistent with a minor, southern splay fault in this area as suggested by Bulut et al. (2012).

The most recent of the focal mechanism earthquakes — on April 4 2019 (M_w 5.3) and December 27 2019 (M_w 4.9) — are each located within ∼5 km of the 2020 Elazığ mainshock epicenter, and so we classify them as foreshocks (Figure 2a,b). Calibrated focal depths along the Pürtürge segment range from 4–18 km with a peak at 10–13 km, in close agreement with our results from elsewhere along the EAF (Supplementary Figure S1c) as well as with previous regional studies (O. Tan et al., 2011; Bulut et al., 2012). These seismogenic layer thicknesses are also consistent with a central EAF locking depth of ∼15 km inferred from satellite geodesy (Walters et al., 2014; Aktug et al., 2016).

3.2 Mainshock coseismic faulting

Coseismic interferograms exhibit a clear surface deformation signal along the Pürtürge segment of the EAF (Figure 3a). Inverting the downsampled data for uniform slip on a single rectangular fault plane reproduced the broad-scale fringe pattern but left prominent residual fringes at the fault tips, especially at the western end in track 123D (Supplementary Figure S2 and Table S7). Solving for two rectangular faults with locations fixed to the mapped trace of the EAF left similarly large residuals at the western end of track 123D (Supplementary Figure S3). However, solving for slip on two rectangular faults with free locations improved the fit in these areas, and so we used this solution as the basis for our distributed slip models (Supplementary Figure S4 and Table S8). The resulting distributed slip, uniform rake model gave rise to root mean square errors of ∼0.44 cm in line-of-sight displacement (Figure 3, Figure S5). Variable rake inversions further reduced residual displacements to ∼0.41 cm but did not improve the fit visually (Figures S6, S7) and so we prefer the simpler model, with distributed slip but uniform rake.

Our preferred geometry comprises two co-linear segments with strike ∼244° and predominantly left-lateral slip, in good agreement with seismological focal mechanisms (Table S9). At the surface, the model faults approximate the mapped trace of the EAF (Duman & Emre, 2013), except that the observed ∼10° fault bend is manifest in our model as a small left stepover. Attempts at fixing the model fault surface projection to match the observed surface trace resulted in worse misfits, and so we consider a stepover to be the best representation of fault structure at the scale of the seismogenic zone. The eastern fault dips steeply (80°) northwards; the western fault dips more gently (64°) northwards and has a small normal component (rake −18°). Maximum slip of 2.4 m occurs at 6–9 km depth but <0.5 m of slip reaches the shallowest slip patches, implying a pronounced shallow slip deficit (Figure 3c). The model moment of 1.79×10^{19} Nm (M_w 6.8) is similar to the largest seismological solution (that of the Global Centroid Moment Tensor project), implying that most the slip inferred from InSAR occurred coseismically.

Our relocated hypocenter lies midway along the eastern model fault segment at a depth of ∼8 km. The earthquake therefore ruptured bilaterally, but with ∼80% of the InSAR model moment occurring WSW of the epicenter. Our back projection results show that high frequency energy is also released almost exclusively WSW of the epicenter, consistent with a rupture velocity in that direction of ∼2 km/s and a rupture duration of ∼20 s (supplementary Figure S8).

3.3 Postseismic displacements

To investigate early postseismic deformation, we processed four consecutive, 6 day, postseismic interferograms on each of the four available tracks (Figure S9). We observe a sharp phase jump localized on the EAF in the earliest postseismic 6 day interferogram (January 27/28 to February 2/3). Although later interferograms suffer from decorrelation, this phase jump seems to have disappeared by the time of the last pair processed (February 14/15 to 20/21).

We used cumulative 24 day interferograms (January 27/28–February 20/21) to estimate early postseismic afterslip, focusing WSW of the mainshock epicenter where coseismic slip was greatest and where InSAR near-field displacements are most coherent (Figure 4a). Fitting fault-perpendicular profiles with the arctan model, we estimate maximum afterslip of ∼13 cm, less than 7% of the peak coseismic slip (Figure 4b and Figure S10). The greatest afterslip occurs close to the mainshock epicenter and appears to be buried, with minimum misfit locking depths of ∼1 km. WSW of the epicenter, afterslip decreases rapidly to ∼3 cm and the locking depth diminishes to near zero, indicating postseismic surface rupturing.

Horizontal coseismic and postseismic displacements mapped with OIC are dominated by topographic artefacts without a clear coseismic signal, although a long-wavelength signal near the fault in the E-W displacement field may reflect left-lateral slip (Supplementary Figure S11). The lack of a distinct coseismic signal at this resolution is consistent with the shallow slip deficit and small amounts of total surface slip inferred from our coseismic and postseismic InSAR models.

3.4 Aftershock seismicity

Most aftershocks exhibit predominantly left-lateral mechanisms along or parallel to the EAF (Figure 2b and Supplementary Tables S10–S11). We observe notable clusters of aftershocks close to the mainshock hypocenter, at the eastern end of the coseismic faulting (west of Lake Hazar), and near the western end (northwest of Pürtürge). In contrast, there is a near absense of aftershocks associated with the peak coseismic slip patch near the intersection of the two InSAR model faults (Figures 2b and 3b). Many of the aftershocks — particularly within the concentrations at either end of the mainshock rupture — lie up to ∼10 km off the main trace of the EAF, suggesting activation of secondary faults within a broad damage zone (Liu et al., 2003). The easternmost aftershock studied here has a distinctive normal component, consistent with interpretations of the Lake Hazar basin as a releasing bend.

Aftershock relocated focal depths range from 7–17 km (Figure S1c) whereas centroid depths from waveform modeling are mostly 2–7 km, with a single deeper event at 20 km. Use of an alternative velocity model (Acarel et al., 2019) in the regional waveform modelling increased centroid depths by on average ∼2 km, reducing but not eliminating the discrepancy with focal depths. These results mimic relations observed in comparably well-instrumented regions elsewhere (Karasözen et al., 2016, 2018; Gaudreau et al., 2019) and likely reflect the depth resolution limitations of both methods, together with the propensity for earthquakes to nucleate deeper within the seismogenic zone and rupture upwards.

4 Discussion

In this section, we first examine the 2020 Elazığ earthquake in the context of structural segmentation, large historical ruptures, and background instrumental seismicity along the central EAF. Second, we discuss characteristics of the 2020 earthquake in light of emerging conceptual models for fault rupture behaviour.

4.1 Relations with previous seismicity and with structural segmentation of the EAF

The Elazığ mainshock nucleated in a zone of apparent structural complexity between the small towns of Uslu and Doğanyol, where Duman and Emre (2013) mapped a pair of small (<500 m) right steps and an abrupt bend in the surface trace of the EAF (Figure 2). The eastern right step, at Uslu, is associated with a ∼1 km fault gap; the western right step, just north of the Karakaya reservoir, is manifest as a ∼4 km stretch of parallel, overlapping fault strands. Just west of these parallel strands, the EAF abruptly changes fault strike by ∼10°. The April 4 and December 27 2019 foreshocks provide further evidence of the structural complexity in this area (Figure 2a). The April 4 M_w 5.3 earthquake appears to have ruptured the EAF close to the eastern fault step at Uslu. The December 27 M_w 4.9 foreshock was located at the fault bend north of Doğanyol; both its nodal planes are at high angles to the EAF, suggesting rupture of a subsidiary structure or splay.

The 2020 mainshock nucleated within this zone of complexity, between and equidistant from the two foreshocks, before rupturing bilaterally towards the ENE and WSW (Figure 2b). The ENE rupture branch terminates at Lake Hazar, interpreted by Cetin et al. (2003) and Duman and Emre (2013) as a left-stepping releasing bend, by Aksoy et al. (2007) as a horst structure, and by Garcia Moreno et al. (2011) as a continuous, unsegmented fault section. The WSW-ward rupture propagated past the ∼10° fault bend — manifest in our simplified slip model as a releasing step — to terminate on a relatively straight section of the fault west of Pürtürge. Here, our model fault geometry is slightly oblique to the mapped surface trace, hinting that at the scale of the seismogenic zone the fault has a somewhat skewed, non-planar geometry (Figure 2b).

Large historical earthquakes in 1874, 1875, 1893 and 1905 are each attributed to the central EAF on the basis of damage patterns and — in one case — reports of surface rupturing (Ambraseys, 1989). The May 3 1874 (M ∼7.1) and March 27 1875 (M ∼6.7) Gölcuk Gölu earthquakes were both centered upon Lake Hazar, whose former name they bear. The 1874 earthquake devastated settlements along a ∼50 km corridor extending from Uslu, ∼15 km SW of the lake, to Tenik, ∼20 km east of it. Surface rupturing is suspected based upon reports that the south side of the lake was uplifted by ∼1–2 m and that the valley NE of the lake was "rent" (Ambraseys, 1989; Ambraseys & Jackson, 1998).

The reported damage distribution hints that faulting may have extended southwest of the lake, too, but this cannot be confirmed. It is therefore uncertain whether the 2020 earthquake ruptured into the slip area of the 1875 earthquake, or stopped short of it. The 1875 earthquake was assigned the same macroseismic epicenter as the 1874 earthquake, but its rupture extents are relatively poorly constrained. The March 2 1893 (M ∼7.1) and December 4 1905 (M_s 6.8) Malatya earthquakes were both centered on the Yarpuzlu restraining bend, with damage focused upon settlements between Erkenek (in the SW) and Pütürge (in the NE) (Ambraseys, 1989). The northeastern limit to the zone of maximum damage in both earthquakes therefore approximates the southwestern limit of faulting in the 2020 earthquake. However, absent of more precise information on the fault extents of the 1893 and 1905 earthquakes, it is unclear whether they are separated from, connected to, or partially overlap with the 2020 rupture area.

Duman and Emre (2013) used the apparent spatial separation between the 1875 and 1893 ruptures to argue for a seismic gap along the Pütürge segment of the EAF. However, our relocation of background seismicity marks the Pütürge segment as amongst the most seismically active sections of the EAF in the past few decades, not normally the hallmark of a supposed seismic gap. During the period 1964–2019, the Pütürge segment hosted eight earthquakes large enough (M_w ∼5) to be ascribed teleseismic focal mechanisms, more than along any other EAF segment (Figure 1b). Similarly, Bulut et al. (2012) observed that during the interval 2007–2011, and discounting the aftershock zone of the 2010 M_w 6.1 Kovancılar earthquake, the densest activity of small-to-moderate events (M_w $> \sim 3$) along the whole EAF occurred between Pütürge and Lake Hazar: the eventual rupture zone of the 2020 earthquake.

4.2 Earthquake behaviour and structural maturity

Our coseismic InSAR modeling suggests that only ∼20% of the peak slip at depth reaches the surficial model fault patches, implying a shallow slip deficit of ∼80% (Figure 3c). Other studies have shown that apparent shallow slip deficits can arise from a lack of resolution in near field InSAR data or from model uncertainties at shallow depth (Xu et al., 2016; Huang et al., 2017). However, in our case, the absence of a clear surface rupturing signal in optical imagery implies that the deficit inferred from InSAR modeling is real.

We consider it unlikely that the shortfall in shallow slip could be recovered by future earthquakes, since most background seismicity is concentrated below 5 km depth (Figure S1c; O. Tan et al. (2011); Bulut et al. (2012)). Early, localized, shallow afterslip is limited to <7% of the maximum coseismic slip magnitude, recovering only a small portion of the deficit (Figure 4). More could be recovered by persistent shallow creep during the interseismic period, especially since serpentinite-rich ophiolitic rocks mapped near the Pürtürge segment could plausibly exhibit velocity-strengthening frictional behavior (Khalifa et al., 2018; Karaoğlan et al., 2013; Yılmaz, 1993). However, afterslip decays rapidly and disappears completely by mid February (Figure S9), inconsistent with persistent creep (e.g., Çakir et al., 2012). Ultimately, longer geodetic time-series are probably required in order to explain in which part of the earthquake cycle the shallow slip deficit is recovered (e.g., Fielding et al., 2009).

Dolan and Haravitch (2014) compared shallow slip deficits of six M_w >7.1 strike-slip earthquakes, and observed that those on immature faults — defined as having cumulative offsets of <25 km — had smaller ratios of surface slip to deep slip (∼50–60%) than those on mature faults (∼85–95%). This is thought to reflect the progressive localization of slip as fault zones evolve over many earthquake cycles, with more of the shallow strain manifest as inelastic, distributed deformation along immature faults (e.g., Kaneko & Fialko, 2011; Zinke et al., 2015; Roten et al., 2017). Earthquakes that are somewhat smaller than the cut-off of M_w 7.1 considered by Dolan and Haravitch (2014) might have even more pronounced shallow slip deficits because of the scaling of moment magnitude with slip area. For example, the 2003 M_w 6.5 Bam earthquake and the 2017 M_w 6.5 Jiuzhaigou earthquake each had very pronounced shallow slip deficits, exhibited minimal postseismic afterslip, and likely ruptured structurally-immature faults (Fialko et al., 2005; Li et al., 2020).

This provides the context by which the rupture characteristics of the Elazığ earthquake may be understood. The central EAF is well-established as of low-to-intermediate structural maturity, with total offsets of ∼9–26 km (Duman & Emre, 2013). This provides a plausible explanation for the low (∼20%) ratio of surface slip to peak slip at depth and the small amounts (<13 cm) of observed shallow afterslip. The slow rupture speed of ∼2 km/s can also characterize immature faults (Perrin et al., 2016). Our results also caution that future morphotectonic or paleoseismological studies of the EAF should be undertaken with the awareness that a large proportion of deformation may be distributed away from the main fault trace.

5 Conclusions

The January 24 2020 M_w6.8 Elazığ ruptured bilaterally along the Pürtürge segment of the EAF from a nucleation point near an abrupt, $\sim$10° bend in the fault surface trace. It was preceded by two nearby ($\sim$5 km distance) moderate foreshocks on April 4 and December 27 2019. To the ENE, the mainshock may have propagated into the rupture zone of the 1874 M $\sim$7.1 Gölcuk Gölu earthquake, and it halted in the Lake Hazar basin, previously identified as a major EAF segment boundary. It propagated to the WSW at $\sim$2 km/s and terminated after $\sim$20 s along a straight, structurally-simple section of the Pürtürge fault segment; relations with the 1893 M $\sim$7.1 and 1905 M_s 6.9 Malatya earthquakes are unclear. Overall, these results indicate that previous structural segmentation models of the central EAF are oversimplified and/or that the characteristic earthquake model is inappropriate here. The mainshock rupture is characterized by a pronounced shallow slip deficit, that is only partially recovered through shallow afterslip. These characteristics — as well as the slow rupture propagation speed and abundant off-fault background and aftershock seismicity — probably reflect the low-to-moderate structural maturity of the central EAF. The possibility for significant off-fault deformation should be taken into account in future paleoseismological and morphotectonic studies of the EAF.

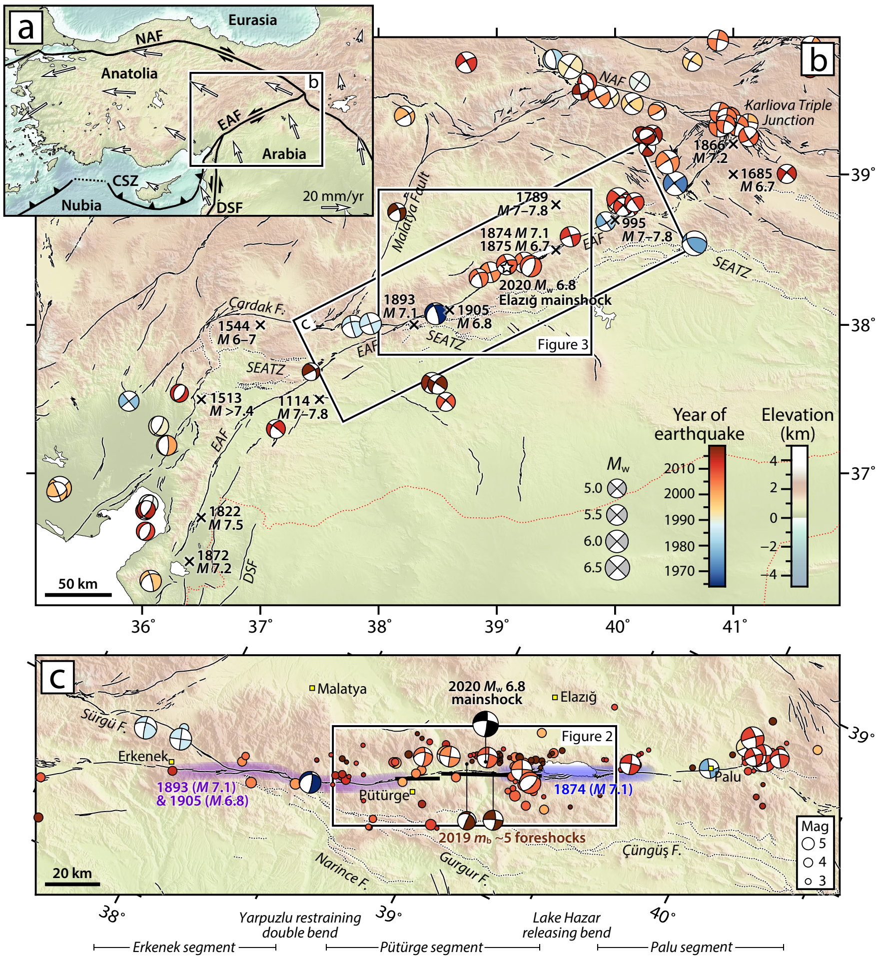

Figure 1. (a) Tectonic setting with plate boundaries (black lines) and representative GPS velocities relative to stable Eurasia (white arrows, from Kreemer et al. (2014)). CSZ = Cyprus Subduction Zone, DSF = Dead Sea Fault, EAF = East Anatolian Fault, NAF = North Anatolian Fault. (b) Focal mechanisms, historical earthquakes, and active faults in SE Anatolia. Teleseismic focal mechanisms, colored by year up to 2019, are from McKenzie (1972), Taymaz et al. (1991) and the USGS and GCMT catalogs. We use our own, relocated epicenters along the EAF and ISC-EHB epicenters elsewhere (Weston et al., 2018). Crosses show macroseismic epicenters of historical EAF earthquakes (Ambraseys, 1989; Ambraseys & Jackson, 1998). Solid lines are strike- or oblique-slip faults and dotted lines are (mostly N-dipping) reverse faults (Emre et al., 2018). SEATZ = Southeast Anatolia Thrust Zone. (c) Close-up of the central EAF. Colored shading shows zones of maximum damage associated with historical earthquakes in 1874 (blue) and 1893 and 1905 (purple), from Ambraseys (1989). Focal mechanisms are as in (b) with the addition of two 2019 foreshocks and the 2020 Elazığ mainshock. Circles show earthquakes without focal mechanisms, colored the same but scaled differently. Thick black lines are surface projections of our preferred InSAR model faults for the 2020 mainshock. Below the map, we show the central EAF segmentation scheme of Duman and Emre (2013).

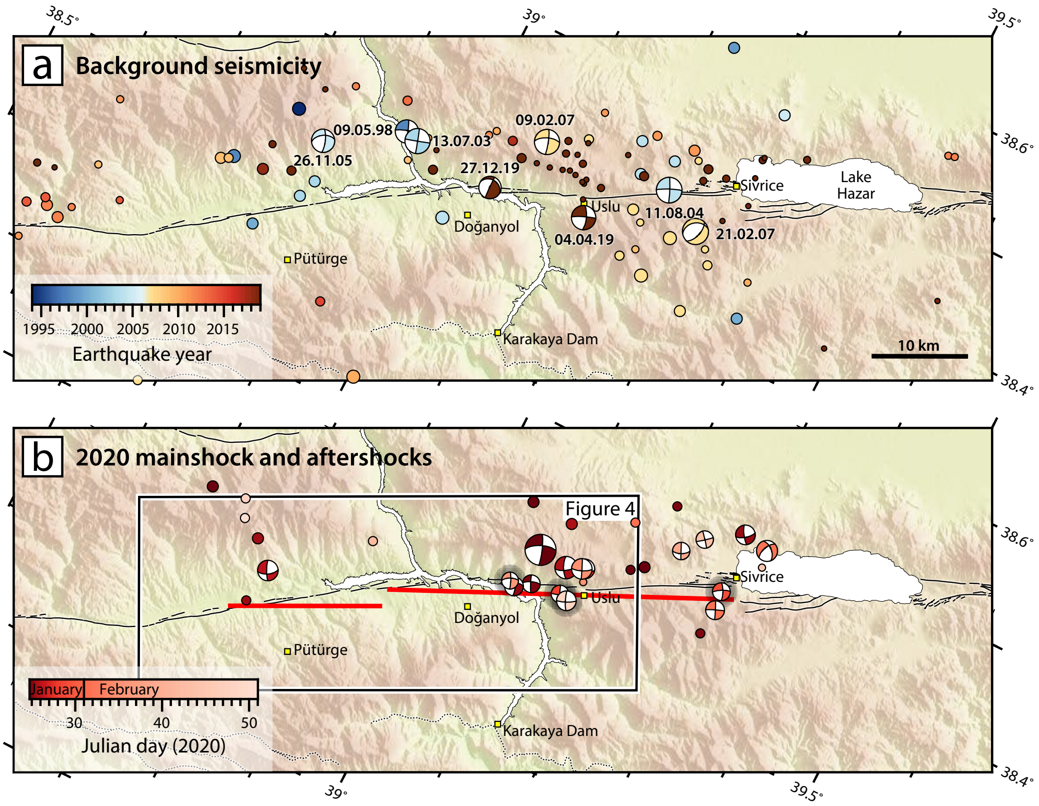

Figure 2. (a) Background seismicity (1994–2019) along the central and eastern Pürtürge segment of the EAF, plotted at relocated epicenters, colored by year, and scaled by magnitude as in Figure 1c. Focal mechanisms are from the GCMT and KOERI catalogs. Faults are as in Figure 1b–c. (b) Elazığ mainshock and aftershock seismicity, plotted at our relocated epicenters where possible (shadowed mechanisms are plotted at EMSC locations) and colored by date. The mainshock mechanism is from the GCMT catalog; aftershock mechanisms are from our own regional waveform modeling. Thick red lines are surface projections of our preferred InSAR model faults for the 2020 Elazığ mainshock.

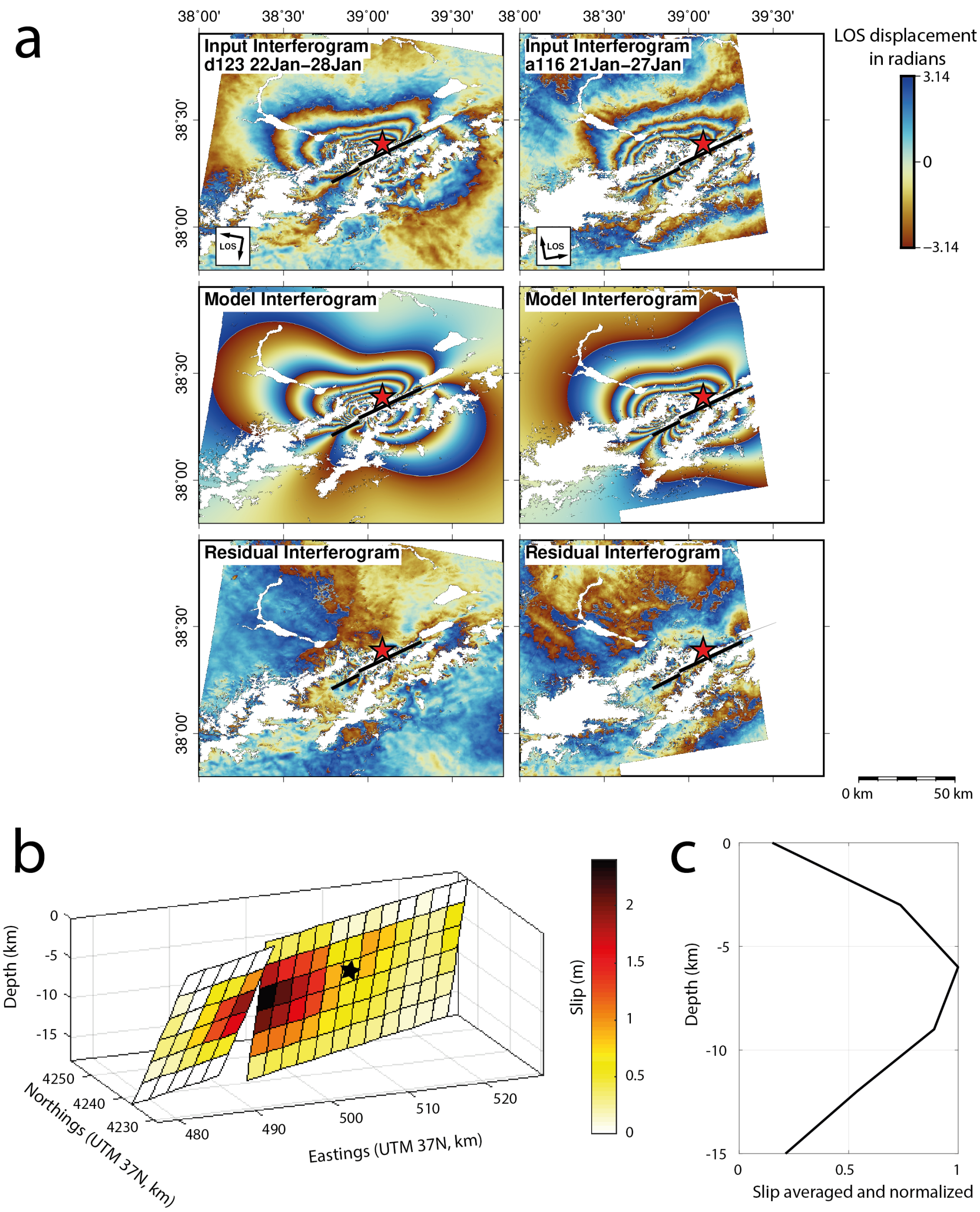

Figure 3. (a) Top: Sentinel-1 interferograms on track track 123D (left) and 116A (right). Middle: model interferograms for our preferred two segment, distributed slip, uniform rake fault models. Bottom: residual interferograms. The thick black line is the surface projection of the modeled fault segments and the red star is the relocated epicenter. Interferograms from tracks 21D and 43A are plotted in supporting information in Figure S5. (b) Model slip distribution. Each fault patch measures 3 × 3 km. The black star shows the relocated hypocenter at 8 km depth, projected on the fault plane. (c) Distribution of normalized average slip versus depth.

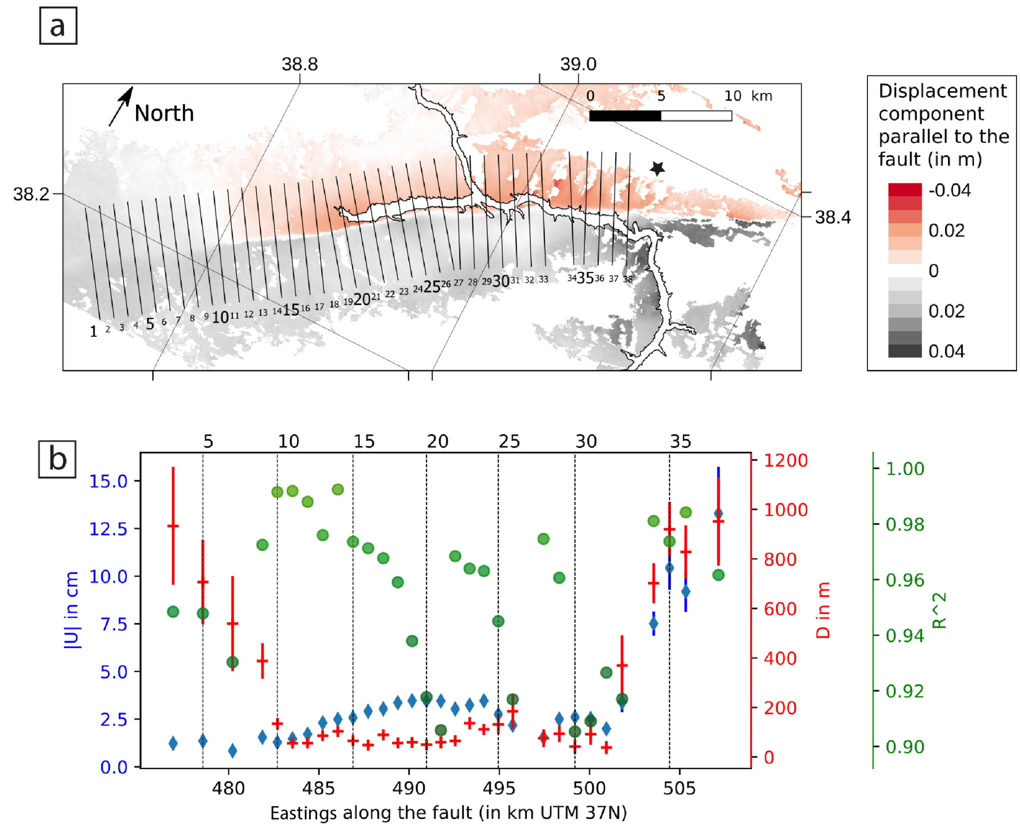

Figure 4. (a) Horizontal displacements projected onto the fault-parallel direction (244°) during the early postseismic period (January 27–February 21 2020), estimated from the A116, A43 and 123D interferograms. Profile lines 1 to 38 are used to fit our afterslip model (profiles with less than 25% of no data values). Observed and modeled displacements are plotted in Figure S10. (b) Afterslip modeling results. Blue diamonds are slip U, red crosses are locking depth D, and green dots show coefficients of determination R^2 (only results with $R^2 > 0.9$ are shown). Vertical dashed lines labelled with numbers (5, 10, etc.) refer to profile numbers displayed in (a). The black star is the relocated epicenter.

Acknowledgments

The University of Victoria Earthquakes group are supported by grants from the Natural Sciences and Engineering Research Council of Canada (NSERC Discovery Grant 2017-04029), the Canada Foundation for Innovation, and the BC Knowledge Development Fund. E. N. is further supported by a Canada Research Chair and E. G. by an NSERC Alexander Graham Bell Canada Graduate Scholarship. All data used in this study are freely available through the links listed below. Interferograms were constructed from Copernicus Sentinel-1 data (`https://scihub.copernicus.eu/`). Teleseismic waveform data

were obtained from IRIS Data Services, and specifically the IRIS Data Management Center (`https://ds.iris.edu/ds/nodes/dmc/`), which are funded through the Seismological Facilities for the Advancement of Geoscience and EarthScope (SAGE) Proposal of the National Science Foundation under Cooperative Agreement EAR-1261681. Regional waveforms were obtained from the Kandilli Observatory and Earthquake Research Institute (`http://eida-service.koeri.boun.edu.tr`). Arrival time data were obtained from the International Seismological Centre Bulletin (`https://doi.org/10.31905/D808B830`). Our relocation clusters have been added to the Global Catalog of Calibrated Earthquake Locations (`https://www.sciencebase.gov/catalog/item/59fb91fde4b0531197b16ac7`), where additional station maps and travel time residual plots are available. Supplementary location parameters were taken from the relocated ISC-EHB dataset (`https://doi.org/10.31905/PY08W6S3`), and we used focal mechanisms from the Global Centroid Moment Tensor project (`https://www.globalcmt.org/`), the United States Geological Survey's Comprehensive Earthquake Catalog (`https://earthquake.usgs.gov/data/comcat/`), and the Kandilli Observatory and Earthquake Research Institute. Many of the figures in this paper were plotted with the *Generic Mapping Tools* software (Wessel et al., 2013).

References

Acarel, D., Cambaz, M. D., Turhan, F., Mutlu, A. K., & Polat, R. (2019). Seismotectonics of Malatya Fault, Eastern Turkey. *Open Geosciences*, *11*(1).

Aksoy, E., Inceoez, M., & Köçyiğit, A. (2007). Lake Hazar basin: A negative flower structure on the east anatolian fault system (EAFS), SE Turkey. *Turk. J. Earth Sci.*, *16*(3), 319–338.

Aktug, B., Ozener, H., Dogru, A., Sabuncu, A., Turgut, B., Halicioglu, K., … Havazli, E. (2016). Slip rates and seismic potential on the East Anatolian Fault System using an improved GPS velocity field. *J. Geodynamics*, *94*, 1–12.

Ambraseys, N. N. (1989). Temporary seismic quiescence: SE Turkey. *Geophys. J. Int.*, *96*(2), 311–331.

Ambraseys, N. N., & Jackson, J. A. (1998). Faulting associated with historical and recent earthquakes in the Eastern Mediterranean region. *Geophys. J. Int.*, *133*, 390–406.

Arpat, E., & Şaroğlu, F. (1972). Some observations and thoughts on the East Anatolian fault. *Bull. Miner. Res. Explor. Inst. Turkey*, *73*, 44–50.

Ayoub, F., Leprince, S., & Avouac, J.-P. (2017). User's guide to COSI-CORR co-registration of optically sensed images and correlation [Computer software manual].

Barka, A. A., & Kadinsky-Cade, K. (1988). Strike-slip fault geometry in Turkey and its influence on earthquake activity. *Tectonics*, *7*(3), 663–684.

Bergman, E. A., & Solomon, S. C. (1990). Earthquake swarms on the Mid-Atlantic Ridge — Products of magmatism or extensional tectonics? *J. Geophys. Res.*, *95*, 4943–4965.

Bouchon, M. (1981). A simple method to calculate Green's functions for elastic layered media. *Bull. Seismol. Soc. Am.*, *71*(4), 959–971.

Boğaziçi University Kandilli Observatory and Earthquake Research Institute. (2001). *International Federation of Digital Seismograph Networks. Dataset/Seismic Network.* doi: 10.7914/SN/KO

Bozkurt, E. (2001). Neotectonics of Turkey — a synthesis. *Geodinamica Acta*, *14*(1), 3–30.

Bulut, F., Bohnhoff, M., Eken, T., Janssen, C., Kılıç, T., & Dresen, G. (2012). The East Anatolian Fault Zone: Seismotectonic setting and spatiotemporal characteristics of seismicity based on precise earthquake locations. *J. Geophys. Res.*, *117*.

Çakir, Z., Ergintav, S., Özener, H., Dogan, U., Akoglu, A. M., Meghraoui, M., & Reilinger, R. (2012). Onset of aseismic creep on major strike-slip faults. *Geology*, *40*(12), 1115–1118.

Cetin, H., Güneyli, H., & Mayer, L. (2003). Paleoseismology of the Palu-Lake Hazar segment of the East Anatolian Fault Zone, Turkey. *Tectonophys.*, *374*(3), 163–197.

Clarke, P. J., Paradissis, D., Briole, P., England, P. C., Parsons, B. E., Billiris, H., ... Ruegg, J.-C. (1997). Geodetic investigation of the 13 May 1995 Kozani-Grevena (Greece) earthquake. *Geophys. Res. Lett.*, *24*, 707–710.

Şengör, A. M. C., & Yilmaz, Y. (1981). Tethyan evolution of Turkey: A plate tectonic approach. *Tectonophys.*, *75*(3), 181–241.

Dolan, J. F., & Haravitch, B. D. (2014). How well do surface slip measurements track slip at depth in large strike-slip earthquakes? The importance of fault structural maturity in controlling on-fault slip versus off-fault surface deformation. *Earth Planet. Sci. Lett.*, *388*, 38–47.

Duman, T. Y., & Emre, O. (2013). The East Anatolian Fault: geometry, segmentation and jog characteristics. In A. H. F. Robertson, O. Parlak, & U. C. Ünlügenç (Eds.), *Geological Development of Anatolia and the Easternmost Mediterranean Region* (Vol. 372, pp. 495–529). Geol. Soc. London Spec. Publ..

Elliott, J. R., Nissen, E. K., England, P. C., Jackson, J. A., Lamb, S., Li, Z., … Parsons, B. (2012). Slip in the 2010-2011 Canterbury earthquakes, New Zealand. *J. Geophys. Res.*, *117*.

Emre, O., Duman, T. Y., Özalp, S., Şaroğlu, F., Olgun, c., Elmacı, H., & Çan, T. (2018). Active fault database of Turkey. *Bull. Earthquake Eng.*, *16*(8), 3229–3275.

Fialko, Y., Sandwell, D., Simons, M., & Rosen, P. (2005). Three-dimensional deformation caused by the Bam, Iran, earthquake and the origin of shallow slip deficit. *Nature*, *435*, 295–299.

Fielding, E. J., Lundgren, P. R., Bürgmann, R., & Funning, G. J. (2009). Shallow fault-zone dilatancy recovery after the 2003 Bam earthquake in Iran. *Nature*, *458*(7234), 64–68.

Garcia Moreno, D., Hubert-Ferrari, A., Moernaut, J., Fraser, J. G., Boes, X., Van Daele, M., … De Batist, M. (2011). Structure and recent evolution of the Hazar Basin: a strike-slip basin on the East Anatolian Fault, Eastern Turkey. *Basin. Res.*, *23*(2), 191–207.

Gaudreau, É., Nissen, E. K., Bergman, E. A., Benz, H. M., Tan, F., & Karasözen, E. (2019). The August 2018 Kaktovik earthquakes: Active tectonics in northeastern Alaska revealed with InSAR and seismology. *Geophys. Res. Lett.*, *46*, 14412–14420.

Huang, M. H., Fielding, E. J., Dickinson, H., Sun, J., Gonzalez-Ortega, J. A., Freed, A. M., & Bürgmann, R. (2017). Fault geometry inversion and slip distribution of the 2010 Mw 7.2 El Mayor-Cucapah earthquake from geodetic data. *J. Geophys. Res.*, *122*(1), 607–621.

Ishii, M., Shearer, P. M., Houston, H., & Vidale, J. E. (2005). Extent, duration and speed of the 2004 Sumatra-Andaman earthquake imaged by the Hi-Net array. *Nature*, *435*, 933–936.

Jackson, J., & McKenzie, D. (1984). Active tectonics of the Alpine-Himalayan Belt between western Turkey and Pakistan. *Geophys. J. Int.*, *77*, 185–264.

Jónsson, S., Zebker, H., Segall, P., & Amelung, F. (2002). Fault Slip Distribution of the 1999 M_w 7.1 Hector Mine, California, Earthquake, Estimated from Satellite Radar and GPS Measurements. *Bull. Seismol. Soc. Am.*, *92*, 1377–1389.

Jordan, T. H., & Sverdrup, K. A. (1981). Teleseismic location techniques and their application to earthquake clusters in the South-Central Pacific. *Bull. Seismol. Soc. Am.*, *71*, 1105–1130.

Kagan, Y. Y., Jackson, D. D., & Geller, R. J. (2012). Characteristic earthquake model, 1884–2011, RIP. *Seismol. Res. Lett.*, *83*(6), 951–953.

Kaneko, Y., & Fialko, Y. (2011). Shallow slip deficit due to large strike-slip earthquakes in dynamic rupture simulations with elasto-plastic off-fault response. *Geophys. J. Int.*, *186*(3), 1389–1403.

Karaoğlan, F., Parlak, O., Klötzli, U., Koller, F., & Rızaoğlu, T. (2013). Age and duration of intra-oceanic arc volcanism built on a suprasubduction zone type oceanic crust in southern Neotethys, SE Anatolia. *Geosci. Frontiers*, *4*(4), 399–408.

Karasözen, E., Nissen, E., Bergman, E. A., Johnson, K. L., & Walters, R. J. (2016). Normal faulting in the Simav graben of western Turkey reassessed with calibrated earthquake relocations. *J. Geophys. Res.*, *121*, 4553–4574.

Karasözen, E., Nissen, E., Büyükakpınar, P., Cambaz, M. D., Kahraman, M., Ertan, E. K., … Özacar, A. A. (2018). The 2017 July 20 M_w 6.6 Bodrum–Kos earthquake illuminates active faulting in the Gulf of Gökova, SW Turkey. *Geophys. J. Int.*, *214*(1), 185–199.

Khalifa, A., Çakir, Z., Owen, L. A., & Kaya, Ş. (2018). Morphotectonic analysis of the East Anatolian Fault, Turkey. *Turk. J. Earth Sci.*, *27*, 110–126.

Kikuchi, M., & Kanamori, H. (1991). Inversion of complex body waves—iii. *Bull. Seismol. Soc. Am.*, *81*(6), 2335–2350.

Kreemer, C., Blewitt, G., & Klein, E. C. (2014). A geodetic plate motion and Global Strain Rate Model. *gcubed*, *15*(10), 3849–3889.

Leprince, S., Barbot, S., Ayoub, F., & Avouac, J.-P. (2007). Automatic and Precise Orthorectification, Coregistration, and Subpixel Correlation of Satellite Images, Application to Ground Deformation Measurements. *IEEE Trans. Geosci.*

Rem. Sens., *45*, 1529–1558. doi: 10.1109/TGRS.2006.888937

Li, Y., Bürgmann, R., & Zhao, B. (2020). Evidence of Fault Immaturity from Shallow Slip Deficit and Lack of Postseismic Deformation of the 2017 Mw 6.5 Jiuzhaigou Earthquake. *Bull. Seismol. Soc. Am.*, *110*(1), 154–165.

Liu, J., Sieh, K., & Hauksson, E. (2003). A Structural Interpretation of the Aftershock "Cloud" of the 1992 M_w 7.3 Landers Earthquake. *Bull. Seismol. Soc. Am.*, *93*(3), 1333–1344.

McKenzie, D. (1972). Active Tectonics of the Mediterranean Region. *Geophys. J. Int.*, *30*, 109–185.

Moré, J. J. (1978). The Levenberg-Marquardt algorithm: Implementation and theory. In G. A. Watson (Ed.), *Numerical analysis* (pp. 105–116). Springer Berlin Heidelberg.

Mulargia, F., Stark, P. B., & Geller, R. J. (2017). Why is Probabilistic Seismic Hazard Analysis (PSHA) still used? *Phys. Earth Planet. Inter.*, *264*, 63–75.

Okada, Y. (1985). Surface deformation due to shear and tensile faults in a half-space. *Bull. Seismol. Soc. Am.*, *75*, 1135–1154.

Parsons, T., & Geist, E. L. (2009). Is There a Basis for Preferring Characteristic Earthquakes over a Gutenberg-Richter Distribution in Probabilistic Earthquake Forecasting? *Bull. Seismol. Soc. Am.*, *99*(3), 2012–2019.

Perrin, C., Manighetti, I., Ampuero, J.-P., Cappa, F., & Gaudemer, Y. (2016). Location of largest earthquake slip and fast rupture controlled by along-strike change in fault structural maturity due to fault growth. *J. Geophys. Res.*, *121*, 3666–3685.

Press, W. H., Teukolsky, S. A., Vetterling, W. T., & Flannery, B. P. (1992). *Numerical recipes in c: The art of scientific computing.* Cambridge: Cambridge University Press.

Roten, D., Olsen, K., & Day, S. (2017). Off-fault deformations and shallow slip deficit from dynamic rupture simulations with fault zone plasticity. *Geophys. Res. Lett.*, *44*(15), 7733–7742.

Savage, J. C., & Burford, R. O. (1973). Geodetic determination of relative plate motion in central California. *J. Geophys. Res.*, *78*(5), 832–845. doi: 10.1029/JB078i005p00832

Scott, C., Champenois, J., Klinger, Y., Nissen, E., Maruyama, T., Chiba, T., &

Arrowsmith, R. (2019). The 2016 M7 Kumamoto, Japan, Earthquake Slip Field Derived From a Joint Inversion of Differential Lidar Topography, Optical Correlation, and InSAR Surface Displacements. *Geophys. Res. Lett.*, *46*(12), 6341–6351.

Socquet, A., Hollingsworth, J., Pathier, E., & Bouchon, M. (2019). Evidence of supershear during the 2018 magnitude 7.5 Palu earthquake from space geodesy. *Nat. Geosci.*, *12*(3), 192–199.

Sokos, E., & Zahradník, J. (2013). Evaluating Centroid-Moment-Tensor Uncertainty in the New Version of ISOLA Software. *Seismol. Res. Lett.*, *84*(4), 656–665.

Sokos, E. N., & Zahradník, J. (2008). ISOLA a Fortran code and a Matlab GUI to perform multiple-point source inversion of seismic data. *Computers & Geosciences*, *34*, 967–977.

Stein, R. S., Barka, A. A., & Dieterich, J. H. (1997). Progressive failure on the North Anatolian fault since 1939 by earthquake stress triggering. *Geophys. J. Int.*, *128*, 594–604.

Tan, F., Ge, Z., Kao, H., & Nissen, E. (2019). Validation of the 3-D phase-weighted relative back projection technique and its application to the 2016 M_w 7.8 Kaikōura earthquake. *Geophys. J. Int.*, *217*(1), 375–388.

Tan, O., Pabuçcu, Z., Tapırdamaz, M. C., İnan, S., Ergintav, S., Eyidoğan, H., ... Kuluöztürk, F. (2011). Aftershock study and seismotectonic implications of the 8 March 2010 Kovancılar (Elazığ, Turkey) earthquake ($M_W = 6.1$). *Geophys. Res. Lett.*, *38*(11).

Taymaz, T., EyidoğaAn, H., & Jackson, J. (1991). Source parameters of large earthquakes in the East Anatolian Fault Zone (Turkey). *Geophys. J. Int.*, *106*(3), 537–550.

Tibi, R., Bock, G., Xia, Y., Baumbach, M., Grosser, H., Milkereit, C., ... Zschau, J. (2001). Rupture processes of the 1999 August 17 Izmit and November 12 Düzce (Turkey) earthquakes. *Geophys. J. Int.*, *144*(2), F1–F7.

Walker, R. T., Bergman, E. A., Szeliga, W., & Fielding, E. J. (2011). Insights into the 1968-1997 Dasht-e-Bayaz and Zirkuh earthquake sequences, eastern Iran, from calibrated relocations, InSAR and high-resolution satellite imagery. *Geophys. J. Int.*, *187*, 1577–1603.

Walters, R. J., Parsons, B., & Wright, T. J. (2014). Constraining crustal velocity fields with InSAR for Eastern Turkey: Limits to the block-like behavior of Eastern Anatolia. *J. Geophys. Res.*, *119*(6), 5215–5234.

Wessel, P., Smith, W. H. F., Scharroo, R., Luis, J., & Wobbe, F. (2013). Generic Mapping Tools: Improved Version Released. *Eos Trans. AGU*, *94*, 409–410.

Weston, J., Engdahl, E. R., Harris, J., Di Giacomo, D., & Storchak, D. A. (2018). ISC-EHB: reconstruction of a robust earthquake data set. *Geophys. J. Int.*, *214*(1), 474–484.

Wright, T. J., Lu, Z., & Wicks, C. (2003). Source model for the M_w 6.7, 23 October 2002, Nenana Mountain Earthquake (Alaska) from InSAR. *Geophys. Res. Lett.*, *30*(18).

Wright, T. J., Parsons, B. E., Jackson, J. A., Haynes, M., Fielding, E. J., England, P. C., & Clarke, P. J. (1999). Source parameters of the 1 October 1995 Dinar (Turkey) earthquake from SAR interferometry and seismic bodywave modelling. *Earth Planet. Sci. Lett.*, *172*, 23–37.

Xu, X., Tong, X., Sandwell, D. T., Milliner, C. W. D., Dolan, J. F., Hollingsworth, J., … Ayoub, F. (2016). Refining the shallow slip deficit. *Geophys. J. Int.*, *204*(3), 1867–1886.

Yılmaz, Y. (1993). New evidence and model on the evolution of the southeast Anatolian orogen. *Geol. Soc. Am. Bull.*, *105*(2), 251–271.

Zahradník, J., Serpetsidaki, A., Sokos, E., & Tselentis, G.-A. (2005). Iterative deconvolution of regional waveforms and a double-event interpretation of the 2003 Lefkada earthquake, Greece. *Bull. Seismol. Soc. Am.*, *95*(1), 159–172.

Zinke, R., Dolan, J. F., Van Dissen, R., Grenader, J. R., Rhodes, E. J., McGuire, C. P., … Hatem, A. E. (2015). Evolution and progressive geomorphic manifestation of surface faulting: A comparison of the Wairau and Awatere faults, South Island, New Zealand. *Geology*, *43*(11), 1019–1022.